PHYSICAL REVIEW C **78**, 025209 (2008)

Measurements of the $\gamma^* p \to \Delta$ reaction at low Q^2: Probing the mesonic contribution

S. Stave,[1,*] N. Sparveris,[2,†] M. O. Distler,[3] I. Nakagawa,[1,4,‡] P. Achenbach,[3] C. Ayerbe Gayoso,[3] D. Baumann,[3] J. Bernauer,[3] A. M. Bernstein,[1,§] R. Böhm,[3] D. Bosnar,[5] T. Botto,[1] A. Christopoulou,[2] D. Dale,[4] M. Ding,[3] L. Doria,[3] J. Friedrich,[3] A. Karabarbounis,[2] M. Makek,[5] H. Merkel,[3] U. Müller,[3] R. Neuhausen,[3] L. Nungesser,[3] C. N. Papanicolas,[2] A. Piegsa,[3] J. Pochodzalla,[3] M. Potokar,[6] M. Seimetz,[3,‖] S. Širca,[6] S. Stiliaris,[2] Th. Walcher,[3] and M. Weis[3]
(A1 Collaboration)
[1]*Department of Physics, Laboratory for Nuclear Science and Bates Linear Accelerator Center, Massachusetts Institute of Technology, Cambridge, Massachusetts 02139, USA*
[2]*Institute of Accelerating Systems and Applications and Department of Physics, University of Athens, Athens, Greece*
[3]*Institute für Kernphysik, Johannes Gutenberg-Universität Mainz, D-55099 Mainz, Germany*
[4]*Department of Physics and Astronomy, University of Kentucky, Lexington, Kentucky 40206, USA*
[5]*Department of Physics, University of Zagreb, Croatia*
[6]*Institute Jožef Stefan, University of Ljubljana, Ljubljana, Slovenia*
(Received 14 March 2008; published 14 August 2008)

The determination of nonspherical angular momentum amplitudes in nucleons at long ranges (low Q^2) was accomplished through the $p(\vec{e}, e'p)\pi^0$ reaction in the Δ region at $Q^2 = 0.060$, 0.127, and 0.200 $(\mathrm{GeV}/c)^2$ at the Mainz Microtron with an accuracy for the cross sections of 4%. The results for the dominant transition magnetic dipole amplitude and the quadrupole to dipole ratios have been obtained with an estimated model uncertainty that is approximately the same as the experimental uncertainty. Lattice and effective field theory predictions agree with our data within the relatively large estimated theoretical uncertainties. Phenomenological models are in good agreement with experiment when the resonant amplitudes are adjusted to the data. To check reaction model calculations additional data were taken for center-of-mass energies below resonance and for the $\sigma_{LT'}$ structure function. These results confirm the dominance, and general Q^2 variation, of the pionic contribution at large distances.

DOI: 10.1103/PhysRevC.78.025209 PACS number(s): 13.60.Le, 13.40.Gp, 14.20.Gk

I. INTRODUCTION

Experimental confirmation of the presence of nonspherical hadron amplitudes (i.e., d states in quark models or p wave π-N states) is fundamental and has been the subject of intense experimental and theoretical interest (for reviews see Refs. [1–5]). This effort has focused on the measurement of the electric and Coulomb quadrupole amplitudes ($E2$, $C2$) in the predominantly $M1$ (magnetic dipole-quark spin flip) $\gamma^* N \to \Delta$ transition.

The present low Q^2 experiments add important data to determine the physical basis of long-range nucleon and Δ nonspherical amplitudes. This is the region where pionic effects are predicted to be dominant and appreciably changing. The experiment was carried out at the Mainz Microtron to measure cross sections and extract the resonant multipoles at $Q^2 = 0.060$, 0.127, and 0.200 $(\mathrm{GeV}/c)^2$. The $Q^2 = 0.060$ $(\mathrm{GeV}/c)^2$ point is the lowest Q^2 value probed to date in modern electroproduction experiments. The $Q^2 = 0.200$ $(\mathrm{GeV}/c)^2$ point tests the Q^2 variation and provides a valuable overlap with newly obtained Jefferson Lab data [6]. The $Q^2 = 0.127$ $(\mathrm{GeV}/c)^2$ point tested the background amplitudes and acted as a comparison of results from Mainz and Bates. Aspects of this work are given in Refs. [7,8]. This work includes more of the details and is a complete account of those data and includes previously unpublished data as well.

The present measurements fill in an important gap in the coverage of the Q^2 evolution between the photon point ($Q^2 = 0$) [9,10] and previously published electroproduction experiments at JLab [11–13] for Q^2 from 0.4 to 6.0 $(\mathrm{GeV}/c)^2$, with the exception of good coverage at $Q^2 = 0.127$ $(\mathrm{GeV}/c)^2$ at Bates [14–17] and Mainz [18–20] at $Q^2 = 0.127$, 0.200 $(\mathrm{GeV}/c)^2$ that have been published.

Because the proton has spin 1/2, no quadrupole moment can be measured. However, the Δ has spin 3/2 so the $\gamma^* N \to \Delta$ reaction can be studied for quadrupole amplitudes in the nucleon and Δ. Due to spin and parity conservation in the $\gamma^* N(J^\pi = 1/2^+) \to \Delta(J^\pi = 3/2^+)$ reaction, only three multipoles can contribute to the transition: the magnetic dipole ($M1$), the electric quadrupole ($E2$), and the Coulomb quadrupole ($C2$) photon absorption multipoles. The corresponding resonant pion production multipoles are $M_{1+}^{3/2}$, $E_{1+}^{3/2}$, and $S_{1+}^{3/2}$. The relative quadrupole to dipole ratios are $\mathrm{EMR} = \mathrm{Re}(E_{1+}^{3/2}/M_{1+}^{3/2})$ and $\mathrm{CMR} = \mathrm{Re}(S_{1+}^{3/2}/M_{1+}^{3/2})$. In the quark model, the nonspherical amplitudes in the nucleon

*Current address: Triangle Universities Nuclear Laboratory, Duke University, Durham, North Carolina 27708, USA.
†Current address: Department of Physics, Laboratory for Nuclear Science and Bates Linear Accelerator. Center, Massachusetts Institute of Technology, Cambridge, Massachusetts 02139, USA.
‡Current address: Radiation Laboratory, RIKEN, 2-1 Hirosawa, Wako, Saitama 351-0198, Japan.
§Corresponding author.
‖Current address: University of Bonn, Physikalisches Inst., Nussallee 12, D-53115 Bonn, Germany.

and Δ are caused by the noncentral, tensor interaction between quarks [21,22]. However, the magnitudes of this effect for the predicted $E2$ and $C2$ amplitudes [23] are at least an order of magnitude too small to explain the experimental results (see Fig. 16 below) and even the dominant $M1$ matrix element is $\simeq$30% low [5,23]. A likely cause of these dynamical shortcomings is that the quark model does not respect chiral symmetry, whose spontaneous breaking leads to strong emission of virtual pions (Nambu-Goldstone bosons) [5]. These couple to nucleons as $\vec{\sigma} \cdot \vec{p}$, where $\vec{\sigma}$ is the nucleon spin and $\vec{p}$ is the pion momentum. The coupling is strong in the p wave and mixes in nonzero angular momentum components. Based on this, it is physically reasonable to expect that the pionic contributions increase the $M1$ and dominate the $E2$ and $C2$ transition matrix elements in the low Q^2 (large distance) domain. This was first indicated by adding pionic effects to quark models [24–26], subsequently in pion cloud model calculations [27,28], and recently demonstrated in effective field theory (chiral) calculations [29,30].

II. EQUIPMENT

The $p(\vec{e}, e'p)\pi^0$ measurements were performed using the $A1$ spectrometers at the Mainz Microtron [31]. Electrons were detected in Spectrometer A which used two pairs of vertical drift chambers for track reconstruction and two layers of scintillator detectors for timing information and particle identification. The protons were detected in Spectrometer B which has a detector package similar to Spectrometer A. Spectrometer B also has the ability to measure at up to 10° out-of-plane in the laboratory. Due to the Lorentz boost, this corresponds to a significantly larger value in the center-of-mass frame. The momentum resolution of the spectrometers is 0.01% and the angular resolution at the target is 3 mrad [31]. Details about the spectrometers are available in Ref. [31]. The MAMI B accelerator delivered a longitudinally polarized, continuous, electron beam up to 855 MeV. Beam polarization was measured periodically with a Møller polarimeter [32] to be $\approx$75%. The beam with average current of up to 25 μA was scattered from a liquid hydrogen cryogenic target. The beam energy has an absolute uncertainty of $\pm$160 keV and a spread of 30 keV (FWHM) [31]. The effects of these uncertainties and the various kinematic cuts were studied to estimate an overall systematic uncertainty (see Table I) for the cross sections of 3 to 4%. This was tested with elastic electron-proton scattering and the data agree with a fit to the world data [33] at the 3% level. In addition, a third spectrometer (Spectrometer C) was used throughout the experiment as a luminosity monitor.

III. EXPERIMENTAL METHODOLOGY

The fivefold differential cross section for the $p(\vec{e}, e'p)\pi^0$ reaction is written as five twofold differential cross sections with an explicit ϕ^* dependence as [34]

$$\frac{d^5\sigma}{d\Omega_f dE_f d\Omega} = \Gamma(\sigma_T + \epsilon\sigma_L + v_{LT}\sigma_{LT}\cos\phi^*_{\pi q} + \epsilon\sigma_{TT}\cos 2\phi^*_{\pi q} + hp_e v_{LT'}\sigma_{LT'}\sin\phi^*_{\pi q}), \quad (1)$$

TABLE I. Summary of systematic and model uncertainties.

Uncertainty	Size (%)
Luminosity	2
Detector inefficiency correction	1
Dead time correction uncertainty per setup	<0.5
Phase-space cut uncertainty	1.5–2.4
Model uncertainty	0.4,1.3
Beam current luminosity correction	0,1
Momentum and angular resolution	1
Beam position	1
Total in quadrature	3.3–3.7
Beam polarization	1.2

where $\phi^*_{\pi q}$ is the pion center-of-mass azimuthal angle with respect to the electron scattering plane, h is the helicity of the electron beam, p_e is the polarization of the electron beam, $v_{LT} = \sqrt{2\epsilon(1+\epsilon)}$, $v_{LT'} = \sqrt{2\epsilon(1-\epsilon)}$, ϵ is the transverse polarization of the virtual photon, and Γ is the virtual photon flux. The virtual photon differential cross sections $(\sigma_T, \sigma_L, \sigma_{LT}, \sigma_{TT}, \sigma_{LT'})$ are all functions of the center-of-mass energy W, the four-momentum transfer squared Q^2, and the pion center-of-mass polar angle $\theta^*_{\pi q}$ (measured from the momentum transfer direction). They are bilinear combinations of the multipoles [34].

The extraction of the cross sections was performed using three sequential measurements. For the helicity independent cross sections there are three cross sections to extract: $\sigma_0 = \sigma_T + \epsilon\sigma_L$($\epsilon$ was not varied so the two cross sections cannot be separated), σ_{TT}, and σ_{LT}. The three twofold differential cross sections can be extracted algebraically by measuring the fivefold differential cross section at the same center-of-mass energy W, four-momentum transfer squared Q^2, and proton center-of-mass polar angle θ^*_{pq} but different values of the proton azimuthal angle ϕ^*_{pq}. (The proton and pion are back-to-back in the center-of-mass frame leading to the following relations between the angles: $\theta^*_{pq} = 180° - \theta^*_{\pi q}$ and $\phi^*_{pq} = 180° + \phi^*_{\pi q}$.) The sequential kinematic settings then keep W and Q^2 constant by keeping the electron arm (Spectrometer A) unchanged and the proton arm was moved so that θ^*_{pq} remained the same and ϕ^*_{pq} was changed. Using Eq. (1), the three twofold differential cross sections $(\sigma_0, \sigma_{TT}, \sigma_{LT})$ can then be found algebraically from the three measured fivefold cross sections and the ϕ^*_{pq} angles at which they were measured. The fifth twofold differential cross section $\sigma_{LT'}$ was measured by reversing the helicity of the longitudinally polarized electron beam at nonzero (out-of-plane) ϕ^*_{pq} angles. $\sigma_{LT'}$ is sensitive to the background terms and provides another test of the reaction calculations.

Figure 1 shows the kinematic overlap for the sequential ϕ^*_{pq} settings at $Q^2 = 0.060$ (GeV/c)^2. The W overlap is approximately 40 MeV, the $\Delta Q^2 \approx 0.04$ (GeV$^2/c^2$), $\Delta\theta^*_{pq} \approx 10°$, and $\Delta\phi^*_{pq} \approx 40°$. For $Q^2 = 0.200$ (GeV/c)^2, the overlap region is slightly larger due to the larger Lorentz boost but the shapes are qualitatively similar.

Studies of the extraction process showed that the smallest uncertainties and most sensitivity were achieved when the

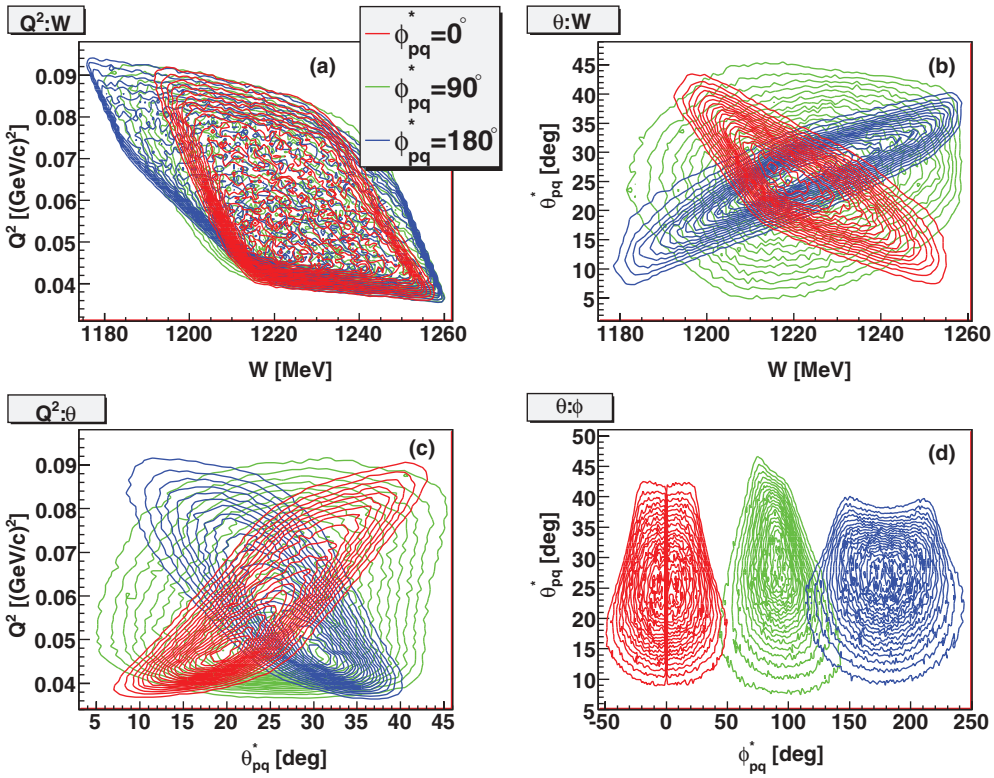

FIG. 1. (Color online) Plot of the overlap of the sequential settings for $Q^2 = 0.060$ (GeV/c)^2, $W = 1221$ MeV, $\theta^*_{pq} = 24^\circ$. Medium gray corresponds to $\phi^*_{pq} = 0^\circ$, light gray to $\phi^*_{pq} = 90^\circ$, and dark gray to $\phi^*_{pq} = 180^\circ$. The amount of overlap for $Q^2 = 0.20$ (GeV/c)^2 is qualitatively similar.

three ϕ^*_{pq} measurements were as far apart as possible. However, at the larger θ^*_{pq} angles, not all ϕ^*_{pq} values can be reached because of the 10° out-of-plane angle constraint of Spectrometer B. Therefore, for each θ^*_{pq} setting, the maximally out-of-plane settings were used. However, each kinematic setting was carefully chosen to minimize the uncertainties in the algebraic cross section extraction process.

The kinematics for all of the setups are shown in detail in Table II. The data presented in this work were taken during two run periods in 2003. The first period was in April and measured the mostly nonparallel cross sections for $Q^2 = 0.060$ and 0.200 (GeV/c)^2 in addition to an extension of the $Q^2 = 0.127$ (GeV/c)^2 data set. The October period was used to measure the W scans at $Q^2 = 0.060$ and 0.200 (GeV/c)^2 and the low W background terms. In addition to the $Q^2 = 0.060, 0.127$, and 0.200 (GeV/c)^2 measurements, some cross-check measurements were made at $Q^2 = 0.127$ (GeV/c)^2 that overlapped with existing data from Bates.

IV. DATA ANALYSIS

A. Phase-space acceptance and simulation

The phase-space acceptance in the spectrometers is in a multidimensional space and has a complex shape (see Fig. 1). One challenge was defining the phase-space acceptance in a similar manner across all the kinematic settings with the phase space varying by a large amount across the spectrometer acceptance. One solution is to have a very small acceptance that will limit the variations but also limit the statistics. Too large

TABLE II. Kinematic values for W, Q^2, proton center-of-mass polar angle θ^*_{pq}, proton azimuthal angle ϕ^*_{pq}, and the initial electron beam energy E_{beam}. See Tables IV and VIII for detailed settings for the W scans.

Q^2 [(GeV/c)^2]	W (MeV)	θ^*_{pq} (°)	ϕ^*_{pq} (°)	E_{beam} (MeV)
0.060	1221	–	$\vec{q}$	795
0.060	1221	24	0.0,90,180	795
0.060	1221	30	29	795
0.060	1221	37	134,180	795
0.200	1221	–	$\vec{q}$	855
0.200	1221	33	0.0,90,180	855
0.200	1221	57	38, 142,180	855
0.060	1125-1300	–	$\vec{q}$	705
0.200	1125-1275	–	$\vec{q}$	855
0.300	1205	–	$\vec{q}$	855
0.060	1155	26	0,180	855
0.127	1140	59	45,135	855
0.127	1221	30,43,63	90,135,150	855
0.127	1212,1232	–	$\vec{q}$	855
0.127	1232	28	0,180	855

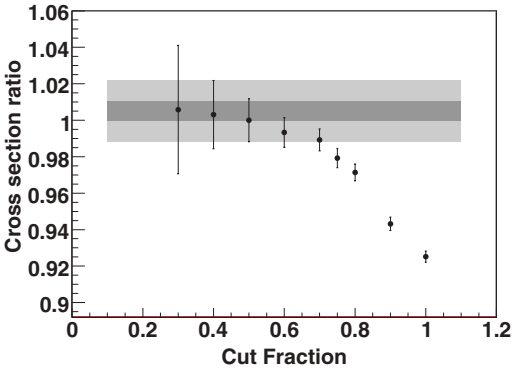

FIG. 2. Variation in the cross section due to changes in cut size for $Q^2 = 0.060$ (GeV/c)^2, $\theta^*_{pq} = 24^\circ$, $\phi^*_{pq} = 0^\circ$. The abscissa shows the fractional phase-space selection width for all the variables mentioned in the text and the ordinate shows the cross section normalized to the cross-section result with the 0.50 fractional phase-space selection width. The bars are centered on the cut corrected result. The dark bar is the statistical uncertainty and the light bar shows the total uncertainty with the systematic uncertainty added in quadrature.

of a phase-space acceptance leads to large systematic errors as the variation in phase space is too large for the simulation to reliably calculate. However, a compromise can be found by settling in a region where the combination of the statistical and systematic errors is a minimum. This is illustrated in Fig. 2 where the normalized cross section is plotted against the size of the kinematic cut. More details of the calculation are presented below but the effect of too small of a phase-space acceptance (large statistical errors on the left side of Fig. 2) can be seen as well as the effect of too large of a phase-space acceptance (large systematic errors seen as deviations from the central value on the right side of Fig. 2).

To ensure uniformity of the phase-space selection across the varying kinematics, a unique solution was found that nonarbitrarily defined the edges of the acceptance. The maximum allowed phase-space region was found by locating the half-maximum points in the distributions of the variables on which the cross section depends: W, Q^2, θ^*_{pq}, ϕ^*_{pq}. Symmetry around the central kinematics was also enforced so that neither side of the phase space was weighted too heavily. Once the maximum acceptance regions were defined, then fractional widths of those regions were used to study the behavior of the extracted cross section. Those studies, detailed below, were then used to define the final phase-space region used for extracting the cross sections.

SIMUL++ [35] is the software that was employed to calculate the multidimensional phase space. SIMUL++ also simulates the collimators inside the spectrometers as part of calculating the phase space. After the subtraction of background events (see next subsection), the spectrometer acceptance was limited in software to the central region of the spectrometers to keep edge effects out of the analysis. The details are in Ref. [36]. In addition to precise spectrometer properties and collimators, SIMUL++ also calculates energy loss and the radiative corrections in the same way as for the data. Each simulated event contains the proper weighting for radiative corrections, the virtual photon flux Γ, and the laboratory to center-of-mass Jacobian. The simulated events undergo kinematic selection processes identical to those used on the data and can then be used to determine the phase space and, finally, a cross section.

Figure 3 shows a comparison of the data for an in-plane, forward setup with the results of SIMUL++ weighted by the MAID 2003 phenomenological model [37] cross section and plotted against the four physics variables on which the cross section depends: W, Q^2, θ^*_{pq}, ϕ^*_{pq}. As is clear in the figure, there is very good agreement for all the variables across the acceptance. A fifth variable, z, was also examined closely because it affects the size of the spectrometer acceptance. z is the vertex position determined by Spectrometer B, which has better vertex resolution than Spectrometer A. The real edges of the z distribution are not as sharp as in the simulation, but extensive studies showed that avoiding those regions in z yielded reliable cross-section results. Other setups have similarly good agreement between data and simulation. In addition to good agreement in the previously listed variables, there is also acceptable agreement on the shape and location of the missing mass peak as shown in Fig. 4. The differences between simulation and data for the missing mass do not cause appreciable uncertainties and the level of agreement is sufficient for this analysis.

To investigate the effects of different-sized phase-space acceptance regions on the extracted cross section, several types of studies were performed. In all of them, the maximum phase-space selection width was defined by the half-maximum points as mentioned earlier. Then, only the fractional width of the phase-space region relative to the maximum width was varied. In this manner, the phase-space selection was consistent across the many kinematic settings.

Fine scans were made for each kinematic setting by simultaneously varying the fractional width of the phase-space selection of all the physics variables (W, Q^2, θ^*_{pq}, ϕ^*_{pq}) and the vertex position, z. (The cross section does not depend on the vertex position but the shape of the vertex distribution did change from setup to setup requiring a similar definition of the cut.) Figure 2 shows the scan for a nonparallel, forward angle, $Q^2 = 0.060$ (GeV/c)^2 setting. The abscissa shows the fractional phase-space selection width for all the variables mentioned and the ordinate shows the cross section normalized to the cross-section result with the 0.50 fractional phase-space selection width. The variation of the cross-section ratio with changing cut fractions seen in Fig. 2 was representative of the variation seen in the other kinematic settings. As mentioned, Fig. 2 shows that the extracted cross section gets more stable with smaller selection regions but the statistical uncertainties necessarily get larger. Small statistical uncertainties are possible with larger cut fractions but then the systematic errors suffer. What is not shown here is that the helicity dependent cross sections have the most stable results for a fractional phase-space selection width of 0.75. The fraction of 0.75 was then chosen as a compromise to have stable results across all kinematics with small statistical uncertainties.

In most settings, like that shown in Fig. 2, the cross section for a fractional phase-space selection width of 0.75 is slightly lower than the 0.50 result. To correct for this, a phase-space

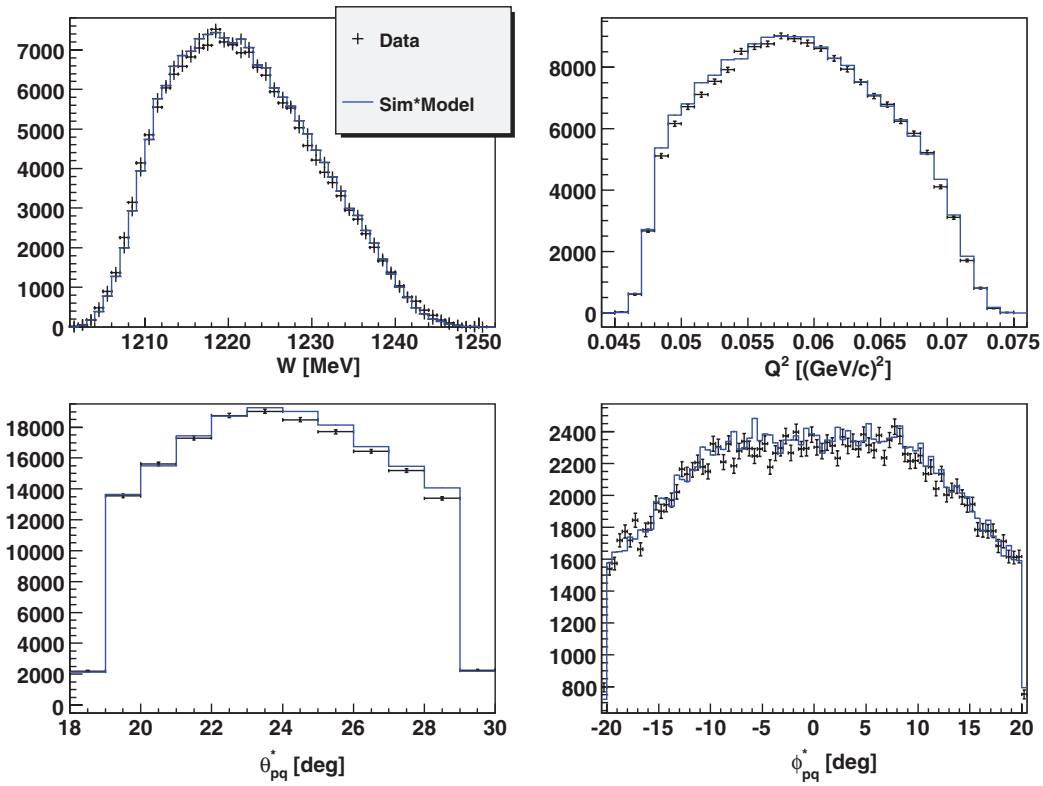

FIG. 3. (Color online) Comparison of the relative shapes in phase space for the data and the simulation weighted by MAID 2003 [37] for the primary variables used in the cut. The results are for an in-plane, forward angle setup at $Q^2 = 0.060$ (GeV/c)^2 and show a good level of agreement.

correction factor was determined by averaging the results of these selection scans over all the similar kinematic settings. These corrections are all on the order of 2 to 3% with a 1% systematic uncertainty. (Some of the backward angle settings had flat phase-space selection width scan results and did not require a phase-space correction factor.) For a comparison of the relative uncertainties, see the light and dark bars in Fig. 2. The light bar shows the statistical uncertainty for the final cross-section result with a fractional phase-space selection width of 0.75 and the dark bar shows the total uncertainty including the appropriate systematic uncertainties. (Because this is a comparison of only one kinematic setting, it is not appropriate to include any uncertainties from quantities that vary statistically or systematically from setup to setup like the luminosity.) The cross-section ratios with fractional phase-space selection widths of 0.50 and 0.75 agree with each other within statistical and systematic uncertainty and are also both stable.

This phase-space selection procedure was used for the analysis of the $Q^2 = 0.060$ (GeV/c)^2 data. Similar cuts were used in the $Q^2 = 0.200$ (GeV/c)^2 analysis and their stability was verified. Any small differences in the cuts lead to only small differences in the cross sections and are not significant.

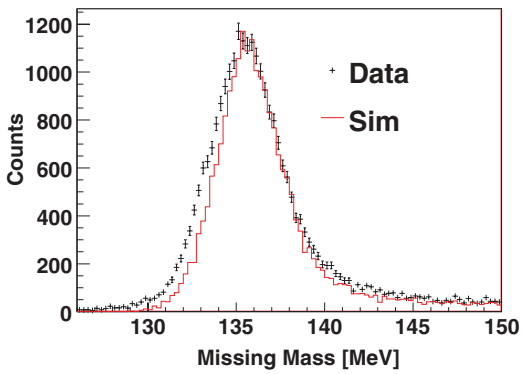

FIG. 4. (Color online) Comparison of the missing mass from the data (black crosses) and the simulation (solid line) for the $Q^2 = 0.060$ (GeV/c)^2, $W = 1221$ MeV, $\theta^*_{pq} = 36^\circ$, $\phi^*_{pq} = 180^\circ$ setting.

B. Elimination of background counts

During the pion production runs, there were two types of backgrounds: π^-/μ^- background and general accidental background. The π^-/μ^- background was removed by making a two-dimensional selection in missing mass versus coincidence timing space. The π^-/μ^- background region was very clearly separated from π^0 events of interest. Their identity was confirmed with a Cherenkov counter in Spectrometer A that was present only during the first running period. However, the two-dimensional selection in missing mass versus coincidence timing space was found to be just as effective at removing the π^-/μ^- background.

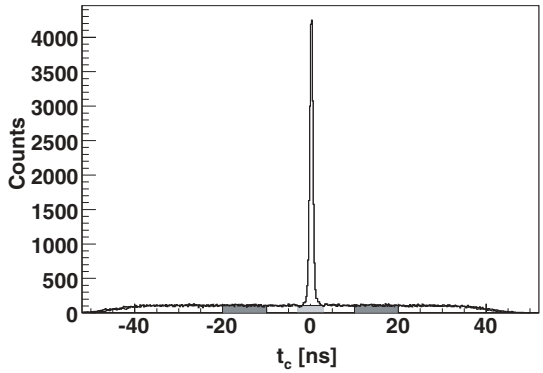

FIG. 5. Coincidence timing of the proton and electron. The dark gray areas indicate the background subtraction region and the light gray under the peak indicates the size of the background. The full-width at half-maximum of the peak is 0.9 ns.

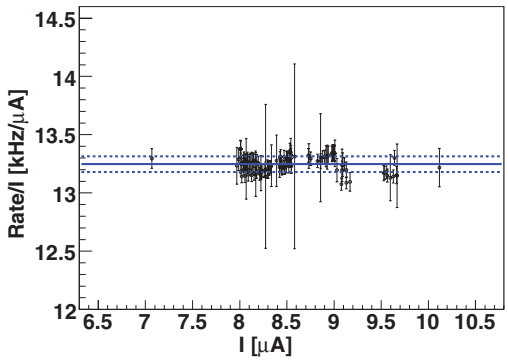

FIG. 6. (Color online) The singles rate in Spectrometer A divided by the beam current for all the $Q^2 = 0.060$ (GeV/c)^2 runs in the April beam time period. The uncertainties shown are statistical only. The lines show the average and RMS deviation of all the data points. Most of the data are within the uncertainties. Even over a range of 3 μA, there is no large target boiling effect.

After the π^-/μ^- cut, an accidental subtraction was applied using accidentals from both sides of the coincidence peak to determine the background counts per channel. Figure 5 shows the coincidence peak on top of the accidental background with the light gray region indicating the average background level seen in the two side regions. The accidental subtraction removes about 6% to 20% of the events in the coincidence peak depending on the kinematics and is the largest of the background subtractions.

After both the pion and accidental background subtractions, the data consist of only coincidence events and a cross section can be extracted that is not contaminated with background events.

C. Luminosity

The luminosity is calculated based on the total current measured by the Förster probe, a pair of toroidal coils that surround the beam and measure the current induced by the beam [38]. The Förster probe is located in the third stage of the microtron that can recirculate the beam up to 90 times. Therefore, the current of the recirculated beam in the third stage can be up to 90 times larger than the beam on target. A measurement there leads to a much more precise determination of the beam current.

The luminosity can then be calculated given the beam current, target length, and target density (from pressure and temperature). To prevent local boiling of the hydrogen target, the electron beam is rasterized or wobbled across the target in a rectangular pattern. During the April run, the beam was also placed off-center to ensure a path to the out-of-plane Spectrometer B that was free of obstructions. The flat plate above the target extended out and would have been in the path of the out-going protons if the beam were not shifted down and to the right. This offset in the beam position decreased the effective target length by less than 1.5% and the effect was taken into account by the simulation.

The normal operating pressure for the target is 2.1 bar. With a normal temperature of 22 K, this leads to an undercooling of 1 K. This temperature buffer allows for a certain amount of local heating without the target starting to boil. However, both pion production run periods experienced lower target pressure that led to less undercooling. Instead of 1 K undercooling, the experiment operated closer to 0.6 K undercooling.

The singles rates in Spectrometer A were used to study the effect of the beam current on the luminosity. (Spectrometer B was rarely in the same place from one setup to another but Spectrometer A was returned to the same location repeatedly.) By plotting the singles rate in A versus beam current, any target boiling effect should be visible. Figure 6 shows the A singles rate divided by the beam current for all the $Q^2 = 0.060$ (GeV/c)^2 runs. Also plotted are the average and the root-mean-square (RMS) deviation of all of the data. Notice that almost all of the points are consistent with a horizontal line that indicates no beam current-dependent luminosity change. Therefore, the low Q^2 runs were below the boiling threshold and do not need any correction.

However, other data were taken with higher beam currents, specifically the parallel pion production cross-section comparison with Bates data and the $Q^2 = 0.200$ (GeV/c)^2 data. It is possible that these runs were taken above the boiling threshold. To test this, the singles rates from Spectrometer A divided by the current was plotted and a line was fit to the data. During the experiment, the effect of the beam current on the luminosity was explicitly checked for one setting where data were taken at 25 μA for 2.5 h and 12.5 μA for 5 h. The results of the fit to the singles data and the beam current study indicate a current dependent effect for beam currents above 12.5 μA. A luminosity correction factor and uncertainty of (3 ± 1)% were adopted that are consistent with all the available data. More details are presented in Ref. [36].

The conclusion from the luminosity studies is that the $Q^2 = 0.06$ (GeV/c)^2 data are unaffected by beam target heating and a (3 ± 1)% correction is sufficient to account for the effect in the remaining data.

D. Extraction at central kinematic values

The analysis procedure yields a cross section that has been averaged over the multidimensional phase space, whereas the

theoretical models provide predicted values at points in that phase space. To compare the averaged cross section to theory, a kinematic translation procedure is applied to the data. This is also known as bin centering corrections [39] or transport. The goal of the procedure is to find the correction factor that will convert the cross section that has been averaged over phase space to the cross section evaluated at the central kinematic values of the phase space. The kinematic correction factor is found by averaging the model predictions over the same volume in phase space as the data. That value is then divided by the model prediction at the center of the phase space. The inverse of that ratio is the correction factor. This technique does not rely on the absolute size of the theory but merely requires that the theory have the same shape throughout the same phase space as the data. Corrections are typically 2 to 3%, indicating that the cross section tends to vary smoothly and fairly symmetrically through the phase space. A small (0.5%) systematic uncertainty is introduced with this method that was estimated by performing the translation with several models and taking the RMS deviation of the results.

This method of translation was tested by varying the size of the phase-space selection region and checking for convergence to the point cross section. Smaller cuts led to larger statistical uncertainties but the tests showed that the results were stable and converged within the uncertainties.

E. Absolute cross section verification

To determine stability over time and the proper normalization, the elastic reaction $p(e, e'p)$ was measured throughout the experiment. As during the pion production runs, Spectrometer A was used to detect electrons and Spectrometer B for protons. The measurement uncertainties are dominated by the systematics estimated at approximately 4%. The results are stable over time and are consistent, within systematic uncertainties, with the 1996 dispersion-theoretical analysis fit to the world elastic data [33]. The 2004 dispersion analysis [40] and other fits to the elastic scattering data [41–44] were examined and there is only a small amount of spread between the fits and they agree at $(98.5 \pm 1.5)\%$ of the 1996 dispersion fit. A more recent dispersion analysis [45] is slightly lower (about 95% of the 1996 fit) but agrees with the other fits and the data within the systematic errors.

The conclusion from the coincidence elastic analysis is that the measured cross sections are stable over time and agree well with previous elastic results. This indicates stability in the luminosity, target density, and beam position. It also indicates that the spectrometers can be placed reliably (typically 0.6 mm and 0.1 mrad [31]) and that the central momenta are well known.

For another check of the absolute cross sections, the parallel pion production cross section at $W = 1232$ MeV and $Q^2 = 0.127$ $(\mathrm{GeV}/c)^2$ was taken during both run times. This measurement had been carried out previously at Bates [15,17,46–48]. The beam energy for each of these past experiments was slightly different and so the ϵ factor is slightly different. This can be corrected for using the ratio of σ_T to σ_L from a model. Using MAID 2003, the correction factor is about 1% and is even smaller for other models. Figure 7 shows all of the parallel cross section comparisons for the previous Bates data and the current experiment. There is a reasonable overlap region because the systematic uncertainties are accounted for in the plot. The Mainz results are stable over time from April 2003 to October 2003. Another item to consider is that the variation in the Bates measurements is about 4% and the difference from Mainz to the lowest Bates point is about the same. The conclusion drawn is that the current measurement agrees with previous measurements within the systematic uncertainties.

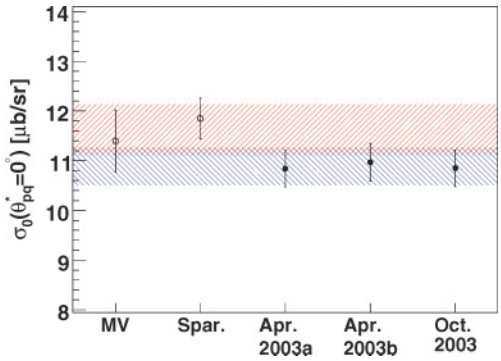

FIG. 7. (Color online) Comparison of the parallel cross section from previous experiments at Bates (○: Mertz-Vellidis (MV) $\epsilon = 0.614$ [15] and Sparveris (Spar.) $\epsilon = 0.768$ [17]) and from the current experiment (●) all measured at or converted to $\epsilon = 0.707$. The uncertainties are the statistical and systematic uncertainties added in quadrature. The / lines are the average of the central values and the uncertainties for Bates. The \ lines are the values for Mainz. The overlap region is easily seen.

F. Systematic uncertainties

As mentioned, the uncertainties from the kinematic translation procedure can be estimated by using various models and looking at the RMS deviation and, for most settings, the effect is less than 0.5%. The one exception is a 1.3% effect due to worse phase-space overlap in the $Q^2 = 0.06\,(\mathrm{GeV}/c)^2$, $\theta_{pq^*} = 29.6^\circ$ setting. This was caused by unforeseen difficulties in placing the spectrometers.

Table I summarizes the remaining uncertainties. The luminosity uncertainty comes from a 1% uncertainty in the target length and a 1% uncertainty in the density. Those estimates have been conservatively added linearly. However, the stability of the elastic cross sections indicates that this systematic uncertainty should affect all runs in the same way. The detector inefficiency correction was estimated in previous works and is quoted here [38,49]. The dead-time correction factor was calculated using vetoed and unvetoed scalers and is based on counting statistics.

The phase-space cut uncertainties were found by varying the size of the kinematic phase space cuts. The large, in-plane angle settings had very little difference, but for the rest of the settings, the difference was typically 2 to 3%. The systematic uncertainty in phase-space cut uncertainties was estimated to be the average of the uncertainties in the ratios of the small

and large cut regions. The systematic uncertainty in the cut correction is between 1.5 and 2.4%.

The model uncertainty in kinematic translation has already been detailed as has the beam current luminosity correction uncertainty. Note that the beam current related luminosity correction is not applied for beam currents less than 12.5 μA and, when it is applied, has a 1% uncertainty.

To see the effect of the spectrometer angular and momentum resolution, the central momentum and angle settings for the spectrometers were shifted in the simulation and the shifted simulation results were used to extract cross sections. Using various combinations of the resolutions and for several, representative setups, the resolution uncertainty was estimated at 1%. The spectrometer positioning uncertainties of 0.6 mm and 0.1 mrad [31] are much smaller than the resolution uncertainties and so do not affect the results. The beam position can also affect the cross section. A study showed that this effect is about 1%.

To summarize, there are several corrections applied to the data (luminosity, phase space, kinematic translation) but they have all been studied in detail and their contributions are all well determined. The total systematic uncertainties are in the range of 3 to 4% and agree very well with the estimates based on comparisons with the world elastic cross sections.

V. EXPERIMENTAL RESULTS

The methods described in the previous sections were applied to the data at $Q^2 = 0.060, 0.127$, and 0.200 (GeV/c)^2 and the results are given here and in the Appendix in tabular form. There are two types of cross sections presented. One is the fivefold differential cross section that is dependent on W, Q^2, θ^*_{pq}, and ϕ^*_{pq} and is measured directly by the spectrometers. The other type is the twofold differential cross section that is ϕ^*_{pq} independent and must be extracted from the fivefold cross sections using Eq. (1). Both types of cross sections are used to aid in comparison with theory and for fitting purposes.

A. Near resonance: $Q^2 = 0.060, 0.200$ (GeV/c)^2

The extracted partial cross sections $\sigma_0, \sigma_{TT}, \sigma_{LT}$, and $\sigma_{LT'}$ versus $\theta^*_{\pi q}$ for $W = 1221$ MeV, $Q^2 = 0.060$ and $W = 1232$ MeV, $Q^2 = 0.200$ (GeV/c)^2 are plotted in Figs. 8 and 9, respectively. These data are compared with the chiral effective field theory calculations (EFT) that have a few low energy parameters and then rely on theory to arrive at results. These calculations have relatively large estimated uncertainty bands due to the neglect of higher-order terms. Within these uncertainties the agreement with experiment is good. Although

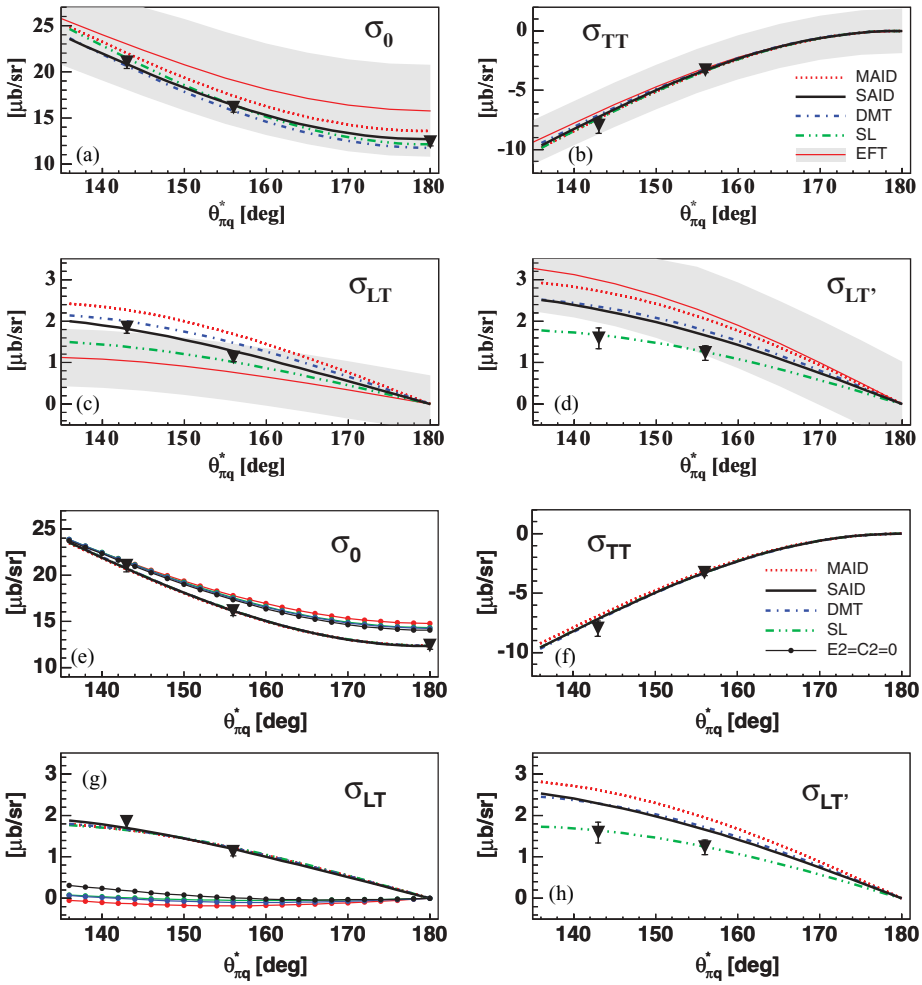

FIG. 8. (Color online) The measured $\sigma_0 = \sigma_T + \epsilon\sigma_L, \sigma_{TT}, \sigma_{LT}$, and $\sigma_{LT'}$ differential cross sections as a function of $\theta^*_{\pi q}$ at $W = 1221$ MeV and $Q^2 = 0.060$ (GeV/c)^2. The ▼ symbols are our data points and include the statistical and systematic uncertainties added in quadrature. The top figures [panels (a)–(d)] show the data with the EFT predictions [30] that are plotted with their estimated uncertainties. The other curves represent predictions from the MAID 2003 [37], SL(Sato-Lee) [27], DMT [28], and SAID [50] models. The bottom figures [panels (e)–(h)] show our data with model curves for which the three resonant multipoles $M^{3/2}_{1+}$, $E^{3/2}_{1+}$, $S^{3/2}_{1+}$ are fit to the data. The lines with dots are the fitted models with the $E^{3/2}_{1+}$ and $S^{3/2}_{1+}$ quadrupole terms set to zero and are plotted only for the sensitive observables, σ_0 and σ_{LT}.

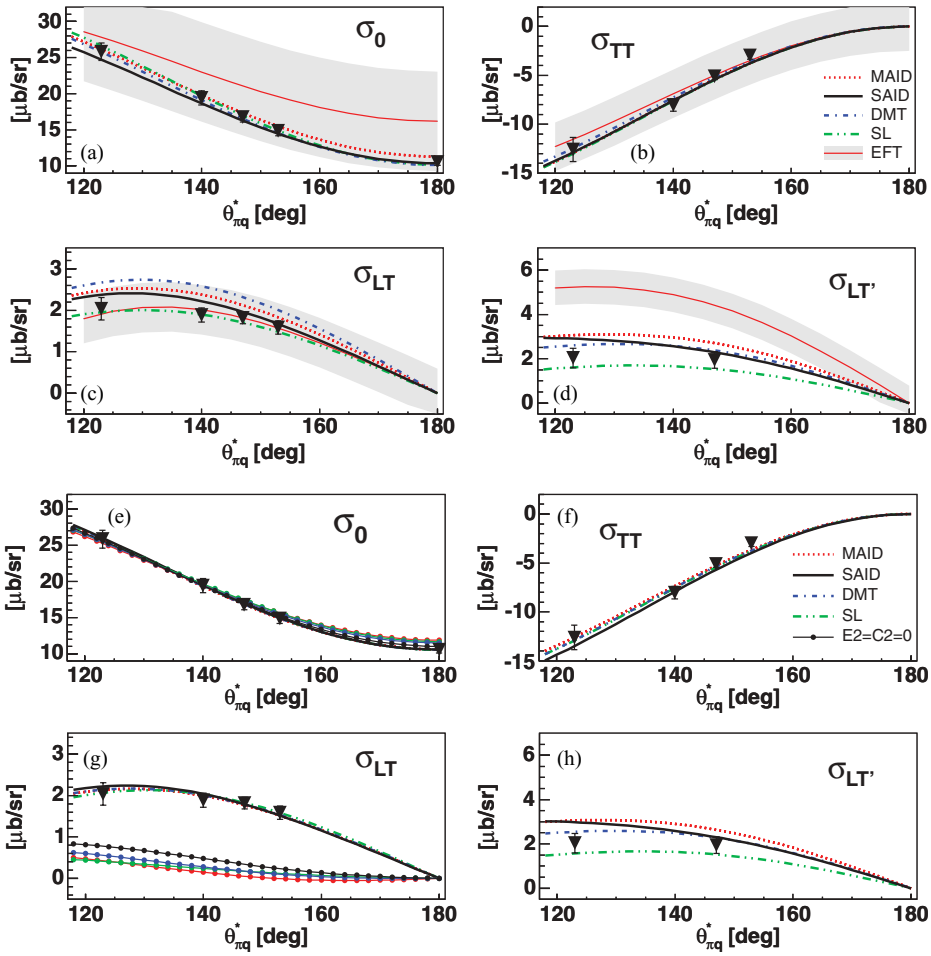

FIG. 9. (Color online) The measured $\sigma_0 = \sigma_T + \epsilon\sigma_L, \sigma_{TT}, \sigma_{LT}$, and $\sigma_{LT'}$ differential cross sections as a function of $\theta^*_{\pi q}$ at $W = 1221$ MeV and $Q^2 = 0.200\,(\mathrm{GeV}/c)^2$. The ▼ symbols are our data points and include the statistical and systematic uncertainties added in quadrature. The top figures [panels (a)–(d)] show the data with the EFT predictions [30] which are plotted with their estimated uncertainties. The other curves represent predictions from the MAID 2003 [37], SL(Sato-Lee) [27], DMT [28], and SAID [50] models. The bottom figures [panels (e)–(h)] show our data with model curves for which the three resonant multipoles $M^{3/2}_{1+}, E^{3/2}_{1+}, S^{3/2}_{1+}$ are fit to the data. The lines with dots are the fitted models with the $E^{3/2}_{1+}$ and $S^{3/2}_{1+}$ quadrupole terms set to zero and are only plotted for the sensitive observables, σ_0 and σ_{LT}.

these calculations and their uncertainty estimates are a great contribution to the field, conclusions cannot be drawn unless there are further improvements. The precision of the data is such that more precise theory is required. The inclusion of even higher-order terms appears to be necessary.

The top sections of Figures 8 and 9 also show the predictions of four model calculations. The Sato-Lee (SL) [27] and Dubna-Mainz-Taipei (DMT) [28] models contain explicit pion cloud contributions, whereas the MAID [37] and SAID [50] calculations are primarily phenomenological. These models have been adjusted by their authors to agree with our previous data [14–17]. For $Q^2 = 0.060\,(\mathrm{GeV}/c)^2$, all models agree with the data for σ_{TT}. For σ_0 only MAID is not in agreement with the data. However, for σ_{LT} the dispersion between the models and data is greater showing that they have not been adjusted to agree with S_{1+}. For $Q^2 = 0.200\ (\mathrm{GeV}/c)^2$, the agreement between models and experiment for S_{1+} is even less satisfactory. One item that this indicates is that the Q^2 dependence of S_{1+} is not correct in DMT and MAID because both models agree well with S_{1+} data at $Q^2 = 0.127\,(\mathrm{GeV}/c)^2$ shown in Ref. [17]. For $\sigma_{LT'}$, only the SL model agrees with the data at both Q^2 values. All of these disagreements show the importance of performing measurements at low Q^2.

The extraction of the three resonant $\gamma^* + p \to \Delta$ amplitudes M_{1+}, E_{1+}, and S_{1+} was accomplished by adjusting these amplitudes in the four phenomenological models described above. Following the practice of Refs. [7,8,15,17] the model-dependent extraction from successful phenomenological reaction models allows for a reliable extraction of the resonant amplitudes. The model uncertainty is estimated by the spread of the derived values using the various model amplitudes [4,51,52].

The fitting procedure used in this analysis is described in detail in Ref. [36]. Briefly, the procedure takes all the background multipoles up to $L = 5$ from a model and varies the amplitude of the resonant, isospin 3/2 multipoles ($M^{3/2}_{1+}$, $E^{3/2}_{1+}$, and $S^{3/2}_{1+}$) to attain a best fit to data at one value of W and Q^2. By performing the fit in this manner, there is not the usual truncation of the fit past p waves. However, there is a model dependence because the various models differ in the sizes of background terms.

The fitting of the data started with the helicity-independent results, the three θ^*_{pq} angles with the ϕ^*_{pq} dependence. Those seven fivefold differential cross section results were fit using the three resonant parameter fit with the four models. All the fits had χ^2 per degree of freedom near one indicating good fits. Correlations between the fitting parameters were taken into account in the uncertainties estimated by the fitting routine [36,53]. Figures 8 and 9 show the data and the different fitted models. Despite different background terms, the four model fits converged. It is impressive that the four model curves almost fall on top of each other when the three resonant $\gamma^* p \to$

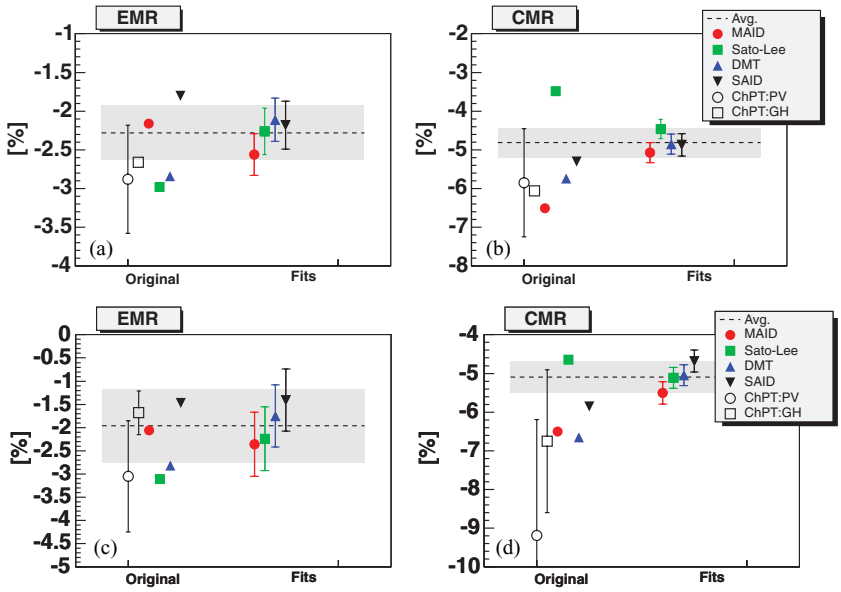

FIG. 10. (Color online) Example of the convergence of the EMR and CMR values with fitting for $W = 1232$ MeV, $Q^2 = 0.06$ (GeV/c)^2 [panels (a)–(b)] and $W = 1232$ MeV, $Q^2 = 0.20$ (GeV/c)^2 [panels (c)–(d)]. The uncertainty on the fits is statistical only since the systematic uncertainty is very small as mentioned in the text. The left side of each plot shows the original model calculations and the right side shows the results after fitting. The gray band is the total statistical, systematic and model uncertainty added in quadrature. The models are MAID 2003 [37,54], DMT [28,55], Sato-Lee [27] and SAID [50]. The chiral effective field theory predictions of Pascalutsa and Vanderhaeghen (PV) [30,56] and Gail and Hemmert (GH) [29] are included.

Δ amplitudes ($M_{1+}^{3/2}$, $E_{1+}^{3/2}$, $S_{1+}^{3/2}$) are varied to fit the data as shown in the lower panel of Figs. 8 and 9. In addition, the lower panels show the "spherical" calculated curves when the resonant quadrupole amplitudes ($E_{1+}^{3/2}$ in σ_0 and $S_{1+}^{3/2}$ in σ_{LT}) are set equal to zero. The difference between the spherical and full curves shows the sensitivity of these cross sections to the quadrupole amplitudes and demonstrates the basis of the present measurement. The small spread in the spherical curves indicates their sensitivity to the model dependence of the background amplitudes.

Figure 10 shows the model convergence for the EMR and CMR at $Q^2 = 0.060$ (GeV/c)^2 in another way. The convergence in M_{1+} was not as significant but the values for M_{1+} have been modified by the various model authors to fit previous data.

It is interesting that good fits were achieved in the resonant region despite the differing model backgrounds. The M_{1+} term is dominant but the background multipoles are of a similar size to the quadrupole E_{1+} and S_{1+} resonant multipoles. The reason that the fitting routine is able to be rather insensitive to the backgrounds is due, mostly, to their having a different phase. Near resonance, the $I = 3/2$ resonant multipoles are mostly imaginary due to the Fermi-Watson theorem [34]. The E_{0+} and S_{0+} are mostly imaginary, whereas others are primarily real. Because the M_{1+} amplitude near resonance is almost pure imaginary, the interference with mostly real amplitudes is very small. In addition, the E_{0+} multipole does not differ very much from model to model so although it has a large effect, it does not affect the resonant fits. The fitting procedure is also insensitive to the background amplitudes partly because of their angular dependence. The primary contributors to the cross section near resonance are the resonant M_{1+}, E_{1+}, and S_{1+} and the background E_{0+} and S_{0+}. The multipole contributions to the cross section have different angular shapes that the fitter can use to separate the components.

As mentioned, in Figures 8 and 9, the $\sigma_{LT'}$ results are close only for the Sato-Lee model but then those cross sections were not included in this fit. The $\sigma_{LT'}$ cross section is sensitive primarily to the background amplitudes and a resonant fit is not expected to improve the agreement. In fact, the fit results were the same, within the uncertainties, whether or not the $\sigma_{LT'}$ data were included.

Table III shows model and chiral EFT predictions along with fitted results for the models and the averages of those models at both Q^2 values. The fits were performed at the same value of W at which the data were taken. The models were then used to extrapolate the value of the multipoles at $W = 1232$ MeV. The table also contains three different types of uncertainties: statistical (used when fitting the data), systematic, and model. The systematic uncertainties are calculated by scaling all of the cross sections to the minimum and maximum allowed by the uncertainties and refitting. The range of the refit values then gives the systematic uncertainty. The systematic uncertainty for the EMR and CMR mostly canceled because the quantities are ratios of multipoles and so are supressed in Table III. However, because $M_{1+}^{3/2}$ is not a ratio, the systematic uncertainties remained. Following our previous work [4,17,51,52], the model uncertainties were found by taking the root-mean-square deviation of the results using the four models. We believe that this is reasonable because the chosen models represent state-of-the-art calculations and also a variety of different approaches. The final statistical and systematic uncertainties are the average over the four models. The model uncertainties and experimental uncertainties are very similar in size, especially for the EMR and CMR, as also seen at $Q^2 = 0.127$ (GeV/c)^2 in Ref. [17]. Therefore, one can conclude that the current experimental limit has been reached and further gains can be achieved only after improving the models. The effect of background amplitudes on the resonant amplitudes was studied and determined to have an effect approximately the same size as the model to model RMS deviation. This study is detailed in Refs. [36] and [51].

B. Parallel cross section

In Figures 11 and 12, the parallel cross section W scans at $Q^2 = 0.060$ and 0.200 (GeV/c)^2, respectively, are plotted

TABLE III. Values of EMR, CMR, and M_{1+} at $W = 1232$ MeV and $Q^2 = 0.060$ (GeV/c)^2 (top) and $Q^2 = 0.200$ (GeV/c)^2 (bottom) for the EFT predictions and fitted models. The uncertainties are in the order of statistical then systematic. The systematic uncertainties for the individual models' EMR and CMR are suppressed because they are small. For the average, the third number is the model uncertainty defined as the RMS deviation of the results from the four different models. The models are the three resonant parameter fitted SAID [50], MAID [37], Sato-Lee(SL) [27], and DMT [28,55] models at $W = 1232$ MeV (1227.3 MeV for SAID [57]) and $Q^2 = 0.060$ (GeV/c)^2. The EFT predictions are Gail and Hemmert (GH) [29] and Pascalutsa and Vanderhaeghen (PV) [30,56] and are presented without fitting to data.

Q^2 (GeV/c)^2	Model	EMR (%)		CMR (%)		$M_{1+}^{3/2}$ ($10^{-3}/m_{\pi^+}$)	
		Fit	Orig.	Fit	Orig.	Fit	Orig.
0.06	SAID	-2.18 ± 0.31	-1.80	-4.87 ± 0.29	-5.30	$40.81 \pm 0.29 \pm 0.57$	40.72
	SL	-2.26 ± 0.30	-2.98	-4.46 ± 0.25	-3.48	$40.20 \pm 0.27 \pm 0.56$	41.28
	DMT	-2.11 ± 0.28	-2.84	-4.85 ± 0.26	-5.74	$40.78 \pm 0.27 \pm 0.57$	40.81
	MAID	-2.56 ± 0.27	-2.16	-5.07 ± 0.26	-6.51	$39.51 \pm 0.26 \pm 0.57$	40.53
	Avg.	$-2.28 \pm 0.29 \pm 0.01 \pm 0.20$		$-4.81 \pm 0.27 \pm 0.03 \pm 0.26$		$40.33 \pm 0.27 \pm 0.57 \pm 0.61$	
	GH	-2.66		-6.06		41.15	
	PV	-2.88 ± 0.70		-5.85 ± 1.40		39.75 ± 3.87	
0.20	SAID	-1.41 ± 0.67	-1.47	-4.68 ± 0.28	-5.85	$38.89 \pm 0.44 \pm 0.62$	39.85
	SL	-2.24 ± 0.69	-3.11	-5.11 ± 0.27	-4.64	$39.76 \pm 0.43 \pm 0.62$	40.48
	DMT	-1.75 ± 0.67	-2.82	-5.04 ± 0.27	-6.65	$39.84 \pm 0.43 \pm 0.62$	39.65
	MAID	-2.36 ± 0.69	-2.06	-5.50 ± 0.29	-6.50	$39.43 \pm 0.43 \pm 0.62$	39.98
	Avg.	$-1.96 \pm 0.68 \pm 0.01 \pm 0.41$		$-5.09 \pm 0.28 \pm 0.02 \pm 0.30$		$39.57 \pm 0.43 \pm 0.62 \pm 0.40$	
	GH	-1.68 ± 0.47		-6.75 ± 1.85			
	PV	-3.05 ± 1.20		-9.19 ± 3.00		38.22 ± 5.10	

along with corresponding model predictions. In Fig. 11(a), the unmodified models are shown. In Fig. 11(b), the results of the three resonant parameter fit to the previously shown data were used. It is important to note that in Fig. 11, only the helicity-independent, low Q^2 results from Sec. V A have been fit and yet the agreement with the W scan data is improved significantly. However, there is still disagreement with the data near the tails which indicate issues with the model backgrounds.

The model curves in Fig. 12 were made in the same way as those for Fig. 11. Again, even though the W-dependent data were not included in the fit, the models converged noticeably. There are even larger deviations at high W indicating an additional Q^2 dependence to the model background terms that is not accounted for properly. It is hoped that both these sets of W-dependent data will help to constrain the models once the models have been improved.

One property that these data can help determine is the shape of the parallel cross section versus Q^2 in the range from $Q^2 = 0.060$ to 0.200 (GeV/c)^2. The four models (MAID, Sato-Lee, SAID, and DMT) do not have a large variation of the shape of the parallel cross section with Q^2 but they do differ from one another in peak center value and width. This was found by plotting the model predictions versus W for the Q^2 range of the data after normalizing the cross sections to the value at the peak. The same procedure was carried out on the Mainz and Bates data and plotted with the peak normalized DMT model in Fig. 13. To aid in the comparison, fits to the data

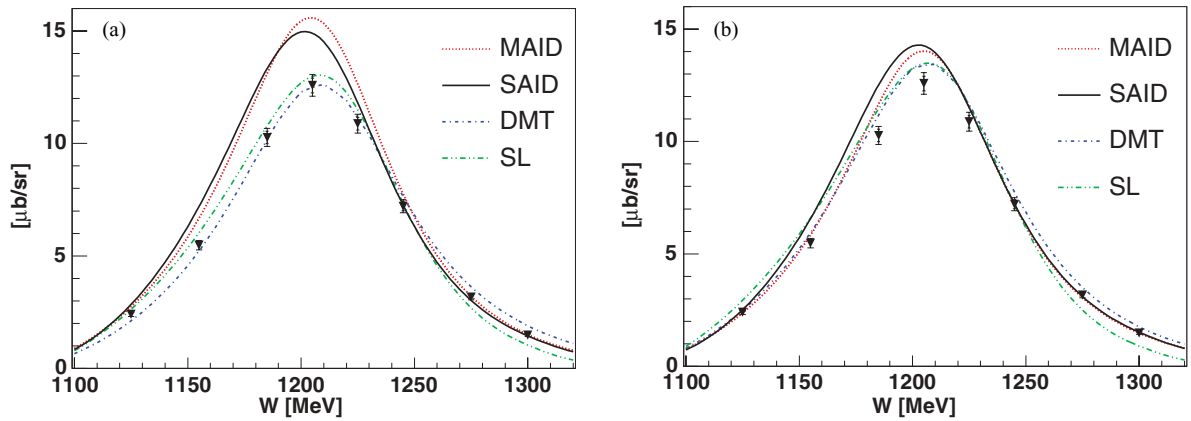

FIG. 11. (Color online) Parallel cross section for the $p(\vec{e}, e' p)\pi^0$ reaction at $Q^2 = 0.060$ (GeV/c)^2 before (a) and after (b) three resonant parameter fit. Model curves are the same as in Fig. 8. The smaller error bars are the statistical uncertainty and the larger error bars include the systematic uncertainty added in quadrature.

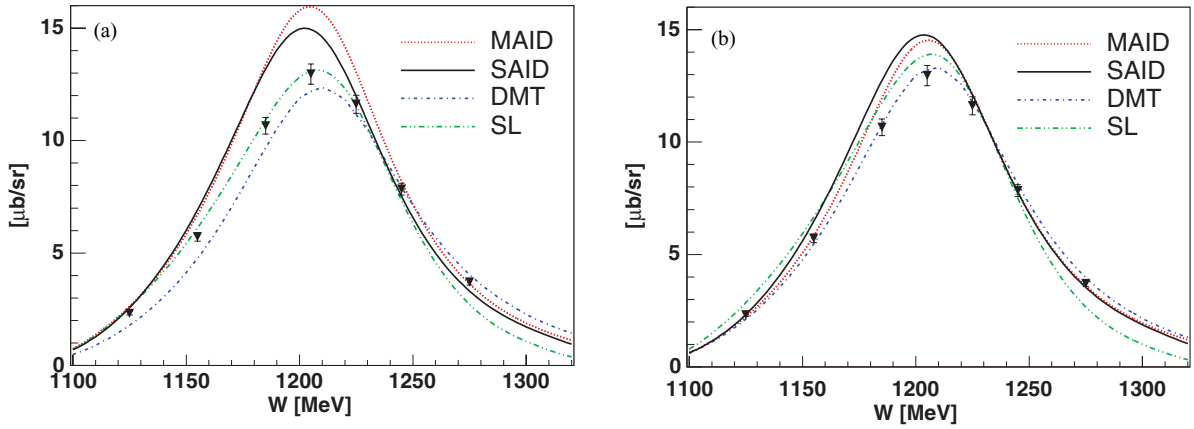

FIG. 12. (Color online) Parallel cross section for the $p(\vec{e}, e'p)\pi^0$ reaction at $Q^2 = 0.200$ (GeV/c)^2 before (a) and after (b) fit. Model curves are the same as in Fig. 8. The uncertainty is the statistical and systematic uncertainties added in quadrature.

were performed using a Breit-Wigner form plus a quadratic background. The fits determined the peak to be $W = 1206 \pm 1$ MeV with widths of 83 to 108 MeV with 10% uncertainties. The shape of the data clearly does not change dramatically. There does appear to be some deviation from the predicted shape toward high W in this model.

In addition to the data taken at $Q^2 = 0.060, 0.127$, and 0.200 (GeV/c)^2, one data point was taken at $Q^2 = 0.300$ (GeV/c)^2. This was a parallel cross-section measurement near the peak of the cross section, $W = 1205$ MeV. As can be seen in Fig. 14, all of the points taken at Mainz are consistent with the unfit Sato-Lee model but show the same variation with Q^2 as all the models. Previous data from Bates [15] tend to have larger values in general as in Fig. 7 but are within the combined uncertainties. The variation with Q^2 is significant because the shape is consistent with a large pion cloud contribution. Note that none of the models in Fig. 14 were fit to the data and the spread in their predicted values is similar to the spread seen in Figs. 11(a)–11(d) and 12(a)–12(d) that also show unfit models.

C. Background-sensitive data below resonance

Background-sensitive data were taken at $Q^2 = 0.060$ (GeV/c)^2 and at low W, where the M_{1+} amplitude is less dominant, to test the background amplitudes in the reaction models. Comparing over a wide range of W is a rigorous test of the background multipoles and the shape of M_{1+}. Also, the background multipoles are more important at low W where they are relatively larger than the resonant multipoles that are then off-resonance. In addition, the M_{1+} term is not purely imaginary in that region and interferences from real background amplitudes will not be suppressed as much. Although the extraction of specific background multipoles was not planned, model predictions can be compared to the data to see whether they agree. In addition, some fitting including background terms can provide an indication as to which amplitudes may be significant. Similar studies were performed in Ref. [17] on the Bates $Q^2 = 0.127$ (GeV/c)^2 data.

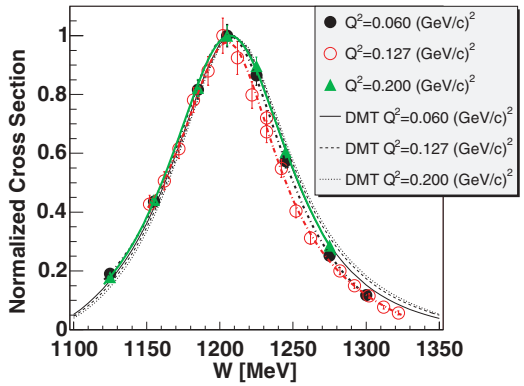

FIG. 13. (Color online) Parallel cross section data (uncertainties are statistical and systematic added in quadrature) for the $p(\vec{e}, e'p)\pi^0$ reaction from Mainz (this article) and Bates [15,17] and model predictions from Ref. [28] scaled so that the $W = 1205$ MeV peak is at 1.0. Note that the shape of the parallel cross does not vary by a large amount. The data points are connected by fits (thick lines) that were a Breit-Wigner form plus a quadratic background.

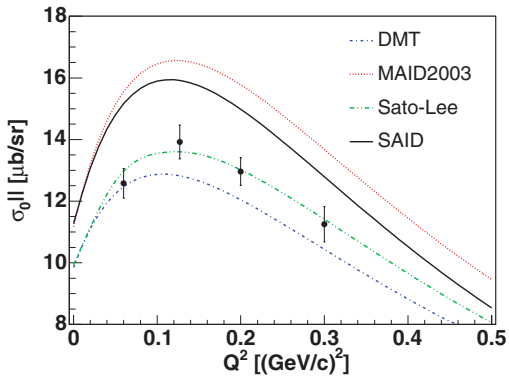

FIG. 14. (Color online) Results for σ_0 versus Q^2 for $W = 1205$ MeV, $\theta^*_{pq} = 0°$. The solid circle data were taken at Mainz and include the statistical and systematic uncertainties added in quadrature. The $Q^2 = 0.127$ (GeV/c)^2 point was taken at $W = 1212$ MeV and models [27,28,37,50] were used to extrapolate to $W = 1205$ MeV. As a result, the uncertainty is slightly larger for that point than the others. The plotted models have not been fit to the data.

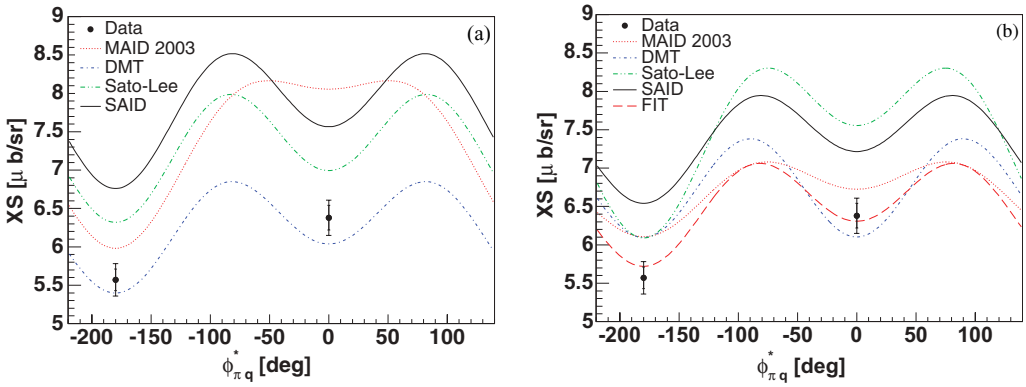

FIG. 15. (Color online) Background sensitive data from Mainz at $W = 1155$ MeV, $Q^2 = 0.060$ (GeV/c)^2 before (a) and after (b) fit to the data near resonance. The smaller error bars are the statistical uncertainty and the larger error bars include the systematic uncertainty added in quadrature. The curves are MAID 2003 (dotted) [37], DMT (dot-dash) [28], Sato-Lee (dot-dot-dash) [27], and SAID (solid line) [50]. Panel (b) also includes an example of one of the four parameter fits (long dash) including these background data. That fit used the three resonant parameters along with M_{1-}) using the MAID 2003 model.

Figure 15 shows the new low W data at $Q^2 = 0.060$ (GeV/c)^2 compared with models before and after fitting the three resonant multipoles at resonance. In Fig. 15(a) only the DMT model is close to the data but does not reproduce both points. The other models differ in size and shape due to their different background amplitudes. The same low W data points are plotted in the lower panel of Fig. 15 along with the model fits at resonance found in Sec. V A. These data points were not included in those fits. The agreement with the models has not improved significantly. This is corroborating the known disagreement among the models for the various background amplitudes.

Taken together, both panels of Fig. 15 indicate that, as expected, more than a three-parameter resonant fit is required away from the resonance region. As an example, one of the best four parameter fits (using the three resonant parameters along with M_{1-}) that include these background data is shown in the lower panel of Fig. 15. Although that fit is satisfactory for the two low W data points, it is still in disagreement with the background-sensitive $\sigma_{LT'}$ data near resonance and for some of the parallel cross section W scan results especially at the low and high W tails. Because of the sensitivity of these few points, the overall χ^2 was not improved very much. However, as mentioned above, because the data set is limited, it is not a surprise that no single background multipole allows a good fit. The effect of background amplitudes from the models can be compared to data but the amplitudes themselves cannot be determined.

Figure 15 indicates the need for more precise model calculations and possible estimates of uncertainties. In addition, dedicated low W experiments could help constrain the models and lead to more refined predictions.

After comparing the data and models over a range of observables, the DMT model has the best overall agreement with all of the low Q^2 data. The fitted DMT result in Fig. 15 is the closest to the data of all the models. The fitted DMT results for $\sigma_{LT'}$ in Fig. 8 are fairly close to the data and no worse than MAID and SAID. Finally, the fitted DMT results for the W scan in Fig. 11 look very good overall and only disagree at a few points. Although no model agrees perfectly with all the data, the DMT model after the three resonant parameter fit does appear to describe the new data the best.

Studies using various fitting parameters indicate a path to follow for improving the agreement between data and theory. The problem encountered with the fitting method used in this work is that the parameters apparently do not give the models enough freedom to fit the background amplitudes. As is clear in the plot in Fig. 11, the models simply have the wrong shape. The next step to constrain the background is to fit the less well determined coupling constants and other internal model terms that affect many multipoles at once. This would hopefully add enough freedom to allow the models to fit the data. Despite these quantitative problems, the background amplitudes are sufficiently small near resonance so the uncertainties in them do not contribute more than the experimental uncertainties in determining the resonant amplitudes.

VI. Q^2 VARIATION OF RESONANT MULTIPOLES

One of the main goals of this experiment is to determine the Q^2 variation of the resonant multipoles. The new Jefferson Lab results [6] for the EMR and CMR at $Q^2 = 0.200$ (GeV/c)^2 agree with our results very well. In addition, it was already shown that the present Mainz data agree with the previous Bates data [15] at $Q^2 = 0.127$ (GeV/c)^2. All of this shows that there is reasonable consistency of the results from the different laboratories.

Figure 16 shows the evolution of the multipoles at low Q^2 along with all the other published points. Two representative constituent quark models, the newer hypercentral quark model (HQM) [60] and an older nonrelativistic calculation of Capstick [23], have been included (the relativistic calculations are in even worse agreement with experiment). These curves are representative of quark models that typically underpredict the dominant $M_{1+}^{3/2}$ multipole by $\simeq$30% and underestimate the EMR and CMR by an order of magnitude, even predicting the wrong sign. One solution to this problem has been to add

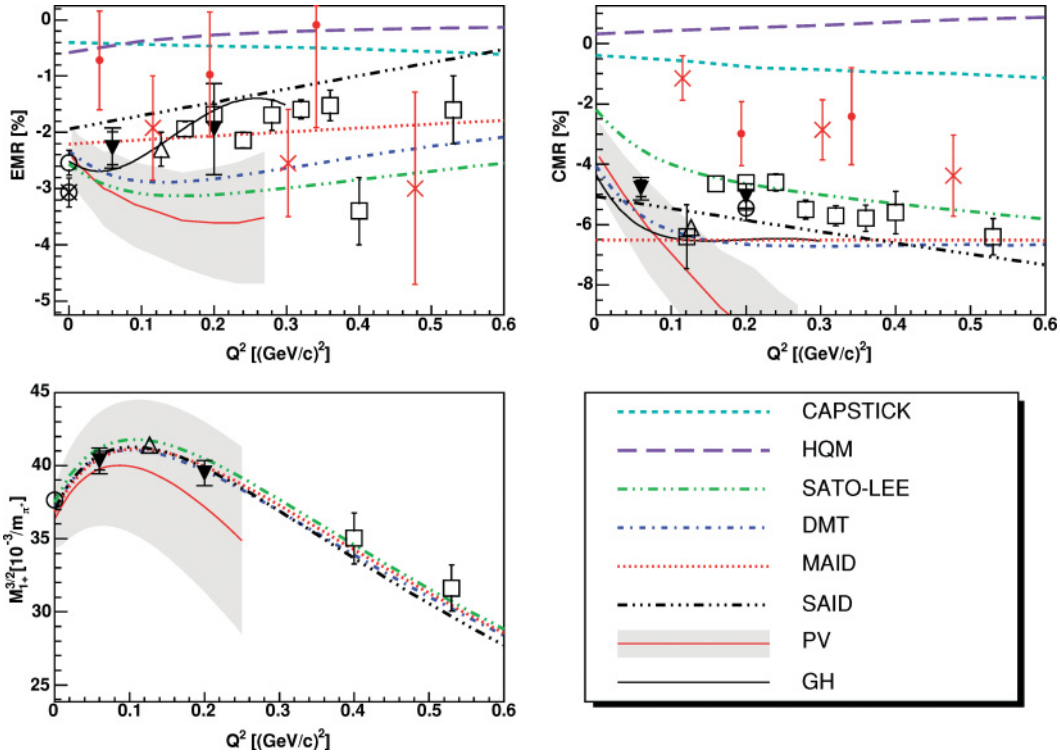

FIG. 16. (Color online) The low Q^2 dependence of the M_{1+}, EMR, and CMR at $W = 1232$ MeV for the $\gamma^* p \to \Delta$ reaction. The ▼ symbols are our data points and include the experimental and model uncertainties (see Table III) added in quadrature. The other data are the photon point data ◯ [9] and ⊗ [10]; CLAS □ [6,11] (CLAS data for $0.16 \leqslant Q^2 \leqslant 0.36$ (GeV/c)^2 are from a unitary isobar model fit and have statistical uncertainties only), Bates △ [17], Elsner ⊕ [20], and Pospischil ⊞; [18]. All uncertainties are statistical and systematic added in quadrature unless otherwise noted. The lattice QCD calculations with linear pion mass extrapolations are shown as × [58] and the new calculations with small pion mass but without extrapolation are shown as • [59]. Also shown are the chiral perturbation calculations of Pascalutsa and Vanderhaeghen (PV) (see EFT in Fig. 8) [30] and Gail and Hemmert (GH) (block solid line) [29]. The other curves represent the same models as in Fig. 8. The HQM (long-dashed line) [60] and Capstick (short-dashed line) [23] quark models have been included.

pionic degrees of freedom to quark models [24–26]. All of these models treat the Δ as a bound state and therefore do not have the π-N continuum (i.e., no background amplitudes) so that cross sections are not calculated. The Sato-Lee [27] and DMT [28] dynamical reaction models with pion cloud effects bridge this gap and are in qualitative agreement with the Q^2 evolution of the data. These models calculate the virtual pion cloud contribution dynamically but have an empirical parametrization of the inner (quark) core contribution that gives them some flexibility in these observables. By contrast the empirical MAID [37] and SAID [50] represent fits to other data with a smooth Q^2 dependence.

Both the dynamical [27,28] and the phenomenological [37,50] models are in qualitative agreement with the experimental results. Nevertheless, all models exhibit some small deficiencies either on top or at the wings of the resonance indicating that detailed improvements could and should be implemented to the models description of resonant or background amplitudes toward accounting for these deficiencies. As a general remark one can note the much better behavior of the dynamical models (DMT and Sato-Lee) compared to the phenomenological ones (MAID and SAID) as far as the description of the W evolution of the cross section is concerned (see Fig. 11), whereas for Sato-Lee the description of the fifth response is also excellent, thus indicating that the model provides the most consistent description of the background amplitudes. One must also point out though the consistent description that SAID provides for the unpolarized cross sections on top of the resonance measurements for all Q^2 points.

The plotted lattice quantum chromodynamics (QCD) results with a linear pion mass extrapolation [58] are in general agreement with the data for the EMR but disagree for the CMR by a wide margin. This margin is bridged, though, when using a chiral extrapolation to the physical pion mass instead of the linear one. The EFT analysis of Pascalutsa and Vanderhaeghen (PV) [30] indicates that a linear extrapolation is close to the data for the EMR but not for the CMR for which these extrapolated lattice results are considerably reduced. The second plotted lattice QCD results were performed with an improved method and a smaller pion mass and are reported without any extrapolation [59]. It is significant that these newer results have the same sign as the data at low Q^2. The general qualitative agreement of the lattice QCD calculation provides a direct link with the experimental evidence for deformation to QCD.

The results of the two effective field theory calculations [29,30] are also presented in Fig. 16. These contain empirical

low-energy constants. For Gail and Hemmert this includes fits to the dominant $M_{1+}^{3/2}$ multipole for $Q^2 \leqslant 0.2$ (GeV/c)^2 and for the EMR at the photon point ($Q^2 = 0$). To achieve the good overall agreement they had to employ one higher-order term with another empirical constant. The EFT calculation of Pascalutsa and Vanderhaeghen [30] provided a valuable estimate of the uncertainties caused by excluding the next higher-order terms from the calculation. Although this is a very helpful start, the uncertainties are significantly larger than the experimental uncertainties and will have to be reduced through a proper treatment of the excluded higher-order terms. However, these effective field theoretical (chiral) calculations that are solidly based on QCD successfully account for the magnitude of the effects giving further credence to the dominance of the meson cloud effect.

One way to see the major role played by the pion cloud contribution to the resonant multipoles is that for this case the expected scale for the Q^2 evolution is $m_\pi^2 = 0.02$ GeV^2. In these units the range of the present experiment for Q^2 from 0.060 to 0.200 (GeV/c)^2 is 3 to 10 units. Therefore it is not surprising that one should see relatively large changes in the predicted Q^2 evolution of the resonant multipoles as is shown in Fig. 16. It is also clear that there is significant model dependence in these predictions.

VII. CONCLUSIONS

The data presented here provide a precise determination of the resonant amplitudes in the $\gamma^* p \to \Delta$ reaction in the range of $Q^2 = 0.06$ to $Q^2 = 0.20$ (GeV/c)^2 (3 to 10 m_π^2). The experiment at the Mainz Microtron was carefully designed to reach the lowest possible Q^2 to test effective field theory calculations and to probe the regime where pionic effects are predicted to be a maximum and to vary significantly [27,28]. The absolute cross section accuracy at the 4% level was verified with several cross checks. The measurement of the $\sigma_0 = \sigma_T + \epsilon\sigma_T, \sigma_{LT}, \sigma_{TT}$ and $\sigma_{LT'}$ partial cross sections, at center-of-mass energies both on and off resonance, allows for sensitive tests of effective field theory [29,30] and reaction model calculations [27,28,37,50]. These partial cross sections are also important for extracting the resonant multipoles from the data; these are used to test lattice calculations [58,59] and quark models [60,61]. At the present time the experiments are more accurate than both theory and model calculations.

The chiral effective field theory predictions [29,30] agree with our cross section data within the relatively large estimated theoretical uncertainties due to the neglect of higher-order terms. It is clear that a quantitative comparison of these calculations and experiment must wait until the next order calculations are performed. The phenomenologically adjusted models Sato-Lee, DMT, SAID, and MAID [27,28,37,50] are in good agreement with experiment when the resonant amplitudes are adjusted to the data. This allows an accurate extraction of the $M1$, $E2$, and $C2$ resonant multipoles ($M_{1+}^{3/2}$, $E_{1+}^{3/2}$, $S_{1+}^{3/2}$) with an estimated model uncertainty that is approximately the same as the experimental uncertainty. This has been achieved due to the precision of the experimental data and also because of the dominance of the magnetic dipole amplitude M_{1+}; this dominance means that differences in the background amplitudes are not significant near resonance and that the model uncertainties in the determination of the resonant multipoles are comparable with the experimental uncertainties. The differences in the background amplitudes have been demonstrated in our low W data and in $\sigma_{LT'}$ for which the background multipoles play a more significant role. This emphasizes the need for model builders to improve their calculations and also to present their uncertainties, as has been done in the EFT calculations. We have performed our own error estimate by comparing the extracted resonance multipoles using different models.

Comparisons of the measured resonant multipoles as a function of Q^2 show reasonable agreement between experiments at different laboratories. The non-zero values of the quadrupole amplitudes ($E_{1+}^{3/2}$, $S_{1+}^{3/2}$) demonstrate the existence of non-spherical amplitudes in the nucleon and Δ conjectured many years ago on the basis of the non-spherical interaction between quarks [21]. This feature is also present in the lattice calculations [58,59], thus linking the experimental evidence for deformation directly to QCD. Unfortunately, the uncertainties in the present calculations are large, which precludes a quantitative comparison with experiment. We anticipate further advances with calculations at lower quark masses combined with improved chiral calculations which are also just in the beginning [30]. These results show qualitative agreement with the two chiral effective field theory results [29,30]. The uncertainties in these latter two calculations indicate that higher-order terms must be evaluated before a quantitative comparison can be made.

Comparison with representative quark models [60,61] shows that they are not close to the data indicating a deficiency of the underlying physics description while demonstrating that the color hyperfine interaction is inadequate to explain the effect, at least at large distances. Our present understanding is that the long-range (low Q^2) region is dominated by the spontaneous breaking of chiral symmetry in QCD that results in nonspherical pion emission and absorption from the nucleon and Δ [1–5].

Even though experiments are ahead of theory at the present time, future experiments can add to the current understanding by measuring in the $n\pi^+$ and γ channels and by using polarized targets and polarimeters. New data for the γ channel from Mainz are under analysis and should be published soon [62]. Additional low-W data would also give a better handle on the background amplitudes.

ACKNOWLEDGMENTS

We thank L. Tiator, D. Drechsel, T.-S. H. Lee, V. Pascalutsa, M. Vanderhaeghen, T. Gail, T. Hemmert, and L. C. Smith for their assistance with valuable discussions and for sharing their unpublished work. This work is supported at Mainz by the Sonderforschungsbereich 443 of the Deutsche Forschungsgemeinschaft (DFG), U. Athens by the Program PYTHAGORAS of the Greek ministry of Education (cofunded by the European Social Fund and National Resources), and at MIT by the U.S. DOE under Grant No. DE-FG02-94ER40818.

APPENDIX: DATA TABLES

TABLE IV. $Q^2 = 0.060$ (GeV/c)^2 cross sections. The first uncertainty is the statistical uncertainty and the second is the systematic uncertainty. The helicity dependent cross sections are shown in Table V. The uncertainties are statistically dominated for those results. The set of $W = 1155$ MeV results are from the background amplitude test. The lower set of results is the W parallel cross section scan.

W (MeV)	θ^*_{pq} (°)	ϕ^*_{pq} (°)	σ (μb/sr)
1221	0	–	$12.35 \pm 0.09 \pm 0.38$
1221	24	0	$11.65 \pm 0.06 \pm 0.36$
1221	24	90	$18.67 \pm 0.09 \pm 0.58$
1221	24	180	$15.39 \pm 0.07 \pm 0.48$
1221	37	32	$15.67 \pm 0.12 \pm 0.52$
1221	37	134	$23.38 \pm 0.12 \pm 0.73$
1221	37	180	$17.87 \pm 0.08 \pm 0.56$
1155	26	0	$5.57 \pm 0.05 \pm 0.20$
1155	26	180	$6.38 \pm 0.04 \pm 0.23$
1125	0	–	$2.40 \pm 0.02 \pm 0.09$
1155	0	–	$5.48 \pm 0.06 \pm 0.20$
1185	0	–	$10.27 \pm 0.10 \pm 0.39$
1205	0	–	$12.58 \pm 0.11 \pm 0.47$
1225	0	–	$10.88 \pm 0.10 \pm 0.41$
1245	0	–	$7.21 \pm 0.09 \pm 0.27$
1275	0	–	$3.17 \pm 0.04 \pm 0.12$
1300	0	–	$1.48 \pm 0.02 \pm 0.06$

TABLE V. Summary of the extracted values for $\sigma_0, \sigma_{TT}, \sigma_{LT}$, and $\sigma_{LT'}$. The uncertainties in the cross section are the statistical and systematic uncertainty, respectively. See text for details of the uncertainty estimation procedure.

W (MeV)	Q^2 [(GeV/c)^2]	θ^*_{pq} (°)	σ	σ (μb/sr)
1221	0.060	24.0	σ_0	$16.10 \pm 0.17 \pm 0.44$
1221	0.060	24.0	σ_{TT}	$-3.30 \pm 0.22 \pm 0.10$
1221	0.060	24.0	σ_{LT}	$1.12 \pm 0.09 \pm 0.04$
1221	0.060	37.0	σ_0	$21.02 \pm 0.31 \pm 0.58$
1221	0.060	37.0	σ_{TT}	$-7.99 \pm 0.63 \pm 0.20$
1221	0.060	37.0	σ_{LT}	$1.85 \pm 0.13 \pm 0.05$
1155	0.060	26.0	σ_{LT}	$0.22 \pm 0.06 \pm 0.07$
1155	0.060	26.0	$\sigma_0 + \epsilon\sigma_{TT}$	$5.97 \pm 0.11 \pm 0.10$
1221	0.060	24.0	$\sigma_{LT'}$	$1.23 \pm 0.18 \pm 0.04$
1221	0.060	37.0	$\sigma_{LT'}$	$1.59 \pm 0.35 \pm 0.06$

TABLE VI. $Q^2 = 0.127$ (GeV/c)^2 results. The first uncertainty is statistical and the second is the systematic. The helicity-dependent results are in Table VII.

W (MeV)	θ^*_{pq} (°)	ϕ^*_{pq} (°)	σ (μb/sr)
1140	58.6	45	$6.93 \pm 0.08 \pm 0.26$
1140	58.6	135	$5.53 \pm 0.04 \pm 0.21$
1221	30	90	$22.61 \pm 0.16 \pm 0.80$
1221	43	135	$26.97 \pm 0.21 \pm 0.95$
1221	63	150	$29.51 \pm 0.23 \pm 1.04$
1205	0	–	$13.92 \pm 0.11 \pm 0.54$
1232	0	–	$10.89 \pm 0.09 \pm 0.36$

TABLE VII. Summary of the extracted values for σ_0, σ_{LT}, and $\sigma_{LT'}$ at $Q^2 = 0.127$ (GeV/c)^2. The uncertainties in the cross section are the statistical and systematic uncertainty, respectively.

W (MeV)	Q^2 [(GeV/c)^2]	θ^*_{pq} (°)	σ	σ(μb/sr)
1140	0.127	58.6	σ_0	$6.23 \pm 0.12 \pm 0.12$
1140	0.127	58.6	σ_{LT}	$-0.58 \pm 0.10 \pm 0.10$
1140	0.127	58.6	$\sigma_{LT'}$	$0.94 \pm 0.16 \pm 0.04$
1221	0.127	30.0	$\sigma_{LT'}$	$1.84 \pm 0.28 \pm 0.07$
1221	0.127	43.0	$\sigma_{LT'}$	$2.80 \pm 0.51 \pm 0.10$
1221	0.127	63.0	$\sigma_{LT'}$	$1.25 \pm 0.78 \pm 0.05$

TABLE VIII. $Q^2 = 0.200$ (GeV/c)^2 cross-section results. The uncertainties correspond to the statistical and the systematic uncertainties, respectively. The lower set of results is the W parallel cross-section scan.

W (MeV)	θ^*_{pq} (°)	ϕ^*_{pq} (°)	σ (μb/sr)
1221	0	–	$12.29 \pm 0.10 \pm 0.51$
1221	27	0	$12.25 \pm 0.13 \pm 0.46$
1221	27	90	$18.28 \pm 0.16 \pm 0.65$
1221	27	180	$16.94 \pm 0.15 \pm 0.58$
1221	33	0	$12.71 \pm 0.11 \pm 0.43$
1221	33	90	$21.73 \pm 0.18 \pm 0.76$
1221	33	180	$18.09 \pm 0.14 \pm 0.63$
1221	40	0	$13.72 \pm 0.14 \pm 0.52$
1221	40	90	$26.46 \pm 0.21 \pm 0.92$
1221	40	180	$19.28 \pm 0.15 \pm 0.67$
1221	57	38	$23.20 \pm 0.20 \pm 0.81$
1221	57	142	$27.86 \pm 0.21 \pm 0.97$
1221	57	180	$22.75 \pm 0.19 \pm 0.77$
1125	0	–	$2.32 \pm 0.02 \pm 0.08$
1155	0	–	$5.72 \pm 0.04 \pm 0.19$
1185	0	–	$10.66 \pm 0.08 \pm 0.36$
1205	0	–	$12.96 \pm 0.09 \pm 0.44$
1225	0	–	$11.62 \pm 0.08 \pm 0.39$
1245	0	–	$7.84 \pm 0.06 \pm 0.26$
1275	0	–	$3.71 \pm 0.04 \pm 0.12$

TABLE IX. Extracted values for $\sigma_0, \sigma_{TT}, \sigma_{LT}$, and $\sigma_{LT'}$ at $Q^2 = 0.200$ (GeV/c)^2. The uncertainties correspond to the statistical and the systematic uncertainties, respectively.

W (MeV)	Q^2 [(GeV/c)^2]	θ^*_{pq} ($^\circ$)	σ	σ (μb/sr)
1221	0.20	27.0	σ_0	$16.44 \pm 0.19 \pm 0.65$
1221	0.20	27.0	σ_{TT}	$-2.99 \pm 0.15 \pm 0.32$
1221	0.20	27.0	σ_{LT}	$1.66 \pm 0.07 \pm 0.13$
1221	0.20	33.0	σ_0	$18.56 \pm 0.21 \pm 0.68$
1221	0.20	33.0	σ_{TT}	$-5.13 \pm 0.16 \pm 0.31$
1221	0.20	33.0	σ_{LT}	$1.90 \pm 0.06 \pm 0.12$
1221	0.20	40.0	σ_0	$21.48 \pm 0.24 \pm 0.99$
1221	0.20	40.0	σ_{TT}	$-8.08 \pm 0.19 \pm 0.59$
1221	0.20	40.0	σ_{LT}	$1.97 \pm 0.07 \pm 0.15$
1221	0.20	57.0	σ_0	$27.36 \pm 0.49 \pm 1.14$
1221	0.20	57.0	σ_{TT}	$-12.28 \pm 0.66 \pm 1.06$
1221	0.20	57.0	σ_{LT}	$2.10 \pm 0.12 \pm 0.24$
1221	0.20	33.0	$\sigma_{LT'}$	$2.10 \pm 0.22 \pm 0.35$
1221	0.20	57.0	$\sigma_{LT'}$	$2.24 \pm 0.26 \pm 0.41$

TABLE X. $Q^2 = 0.300$ (GeV/c)^2 results. The first uncertainty is statistical and the second is systematic.

W MeV	θ^*_{pq} ($^\circ$)	ϕ^*_{pq} ($^\circ$)	σ (μb/sr)
1205	0	–	$11.25 \pm 0.18 \pm 0.54$

[1] A. M. Bernstein and C. N. Papanicolas, edited by, *Shapes of Hadrons, Athens, Greece, 27–29 April 2006*, edited by C. N. Papanicolas and A. M. Bernstein, AIP Conference Proceedings, Vol. **904** (AIP, New York, 2007).

[2] A. M. Bernstein and C. N. Papanicolas, in *Shapes of Hadrons, Athens, Greece, 27–29 April 2006*, edited by C. N. Papanicolas and A. M. Bernstein, AIP Conference Proceedings, Vol. **904**, (AIP, New York, 2007).

[3] D. Drechsel and L. Tiator, *Proceedings of the Workshop on the Physics of Excited Nucleons*, edited by D. Drechsel and L. Tiator (World Scientific, Singapore, 2001).

[4] C. N. Papanicolas, Eur. Phys. J. A **18**, 141 (2003).

[5] A. M. Bernstein, Eur. Phys. J. A **17**, 349 (2003).

[6] B. Julia-Diaz, T. S. H. Lee, T. Sato, and L. C. Smith, Phys. Rev. C **75**, 015205 (2007).

[7] S. Stave *et al.*, Eur. Phys. J. A **30**, 471 (2006).

[8] N. F. Sparveris *et al.*, Phys. Lett. **B651**, 102 (2007).

[9] R. Beck *et al.*, Phys. Rev. C **61**, 035204 (2000).

[10] G. Blanpied *et al.*, Phys. Rev. C **64**, 025203 (2001).

[11] K. Joo *et al.* (CLAS Collaboration), Phys. Rev. Lett. **88**, 122001 (2002).

[12] V. V. Frolov *et al.*, Phys. Rev. Lett. **82**, 45 (1999).

[13] M. Ungaro *et al.* (CLAS Collaboration), Phys. Rev. Lett. **97**, 112003 (2006).

[14] G. A. Warren *et al.* (MIT-Bates OOPS Collaboration), Phys. Rev. C **58**, 3722 (1998).

[15] C. Mertz *et al.*, Phys. Rev. Lett. **86**, 2963 (2001).

[16] C. Kunz *et al.* (MIT-Bates OOPS Collaboration), Phys. Lett. **B564**, 21 (2003).

[17] N. F. Sparveris *et al.* (OOPS Collaboration), Phys. Rev. Lett. **94**, 022003 (2005).

[18] T. Pospischil *et al.*, Phys. Rev. Lett. **86**, 2959 (2001).

[19] P. Bartsch *et al.*, Phys. Rev. Lett. **88**, 142001 (2002).

[20] D. Elsner *et al.*, Eur. Phys. J. A **27**, 91 (2006).

[21] S. L. Glashow, Physica A **96**, 27 (1979).

[22] N. Isgur, G. Karl, and R. Koniuk, Phys. Rev. D **25**, 2394 (1982).

[23] S. Capstick and G. Karl, Phys. Rev. D **41**, 2767 (1990).

[24] D.-H. Lu, A. W. Thomas, and A. G. Williams, Phys. Rev. C **55**, 3108 (1997).

[25] U. Meyer, E. Hernandez, and A. J. Buchmann, Phys. Rev. C **64**, 035203 (2001).

[26] M. Fiolhais, B. Golli, and S. Širca, Phys. Lett. **B373**, 229 (1996).

[27] T. Sato and T. S. H. Lee, Phys. Rev. C **63**, 055201 (2001).

[28] S. S. Kamalov and S. N. Yang, Phys. Rev. Lett. **83**, 4494 (1999).

[29] T. A. Gail and T. R. Hemmert, Eur. Phys. J. A **28**, 91 (2006).

[30] V. Pascalutsa and M. Vanderhaeghen, Phys. Rev. Lett. **95**, 232001 (2005).

[31] K. I. Blomqvist *et al.*, Nucl. Instrum. Methods A **403**, 263 (1998).

[32] P. Bartsch, Ph.D. thesis, Johannes Gutenberg-Universitaet Mainz, 2001.

[33] P. Mergell, U. G. Meissner, and D. Drechsel, Nucl. Phys. **A596**, 367 (1996).

[34] D. Drechsel and L. Tiator, J. Phys. G **18**, 449 (1992).

[35] M. O. Distler, H. Merkel, and M. Weis, in *Proceedings of the 12th IEEE Real Time Congress on Nuclear and Plasma Sciences, Valencia, Spain, 2001*, edited by E. Sanchis Peris, A. Ferrer Soria, and V. González Millán (IEEE, New York, 2001).

[36] S. Stave, Ph.D. thesis, MIT, 2006.

[37] D. Drechsel, O. Hanstein, S. S. Kamalov, and L. Tiator, Nucl. Phys. **A645**, 145 (1999).

[38] S. Širca, Ph.D. thesis, University of Ljubljana, 1999.

[39] J. R. Arrington, Ph.D. thesis, California Institute of Technology, 1998.

[40] H. W. Hammer and U.-G. Meissner, Eur. Phys. J. A **20**, 469 (2004).

[41] J. Seely (private communication).

[42] E. L. Lomon, Phys. Rev. C **66**, 045501 (2002).

[43] J. Friedrich and T. Walcher, Eur. Phys. J. A **17**, 607 (2003).

[44] G. G. Simon, C. Schmitt, F. Borkowski, and V. H. Walther, Nucl. Phys. **A333**, 381 (1980).

[45] M. A. Belushkin, H. W. Hammer, and U. G. Meissner, Phys. Rev. C **75**, 035202 (2007).

[46] C. Mertz, Ph.D. thesis, Arizona State University, 1998.

[47] C. Vellidis, Ph.D. thesis, University of Athens, 2001.

[48] N. Sparveris, Ph.D. thesis, University of Athens, 2003.

[49] A. W. Richter, Ph.D. thesis, Johannes Gutenberg-Universitaet Mainz, (1994).

[50] R. A. Arndt, W. J. Briscoe, I. I. Strakovsky, and R. L. Workman, Phys. Rev. C **66**, 055213 (2002), http://gwdac.phys.gwu.edu.
[51] S. Stave *et al*., AIP Conf. Proc. **904**, 245 (2007).
[52] E. Stiliaris and C. N. Papanicolas, AIP Conf. Proc. **904**, 257 (2007).
[53] F. James and M. Roos, Comput. Phys. Commun. **10**, 343 (1975).
[54] D. Drechsel, S. Kamalov, and L. Tiator (2006), an online version of the numerical program for Ref. [37] is accessible at http://www.kph.uni-mainz.de/MAID/maid2003/maid2003.html.
[55] S. S. Kamalov, G.-Y. Chen, S.-N. Yang, D. Drechsel, and L. Tiator, Phys. Lett. **B522**, 27 (2001).
[56] V. Pascalutsa and M. Vanderhaeghen, Phys. Rev. D **73**, 034003 (2006).
[57] R. A. Arndt (private communication).
[58] C. Alexandrou, P. deForcrand, H. Neff, J. W. Negele, W. Schroers, and A. Tsapalis, Phys. Rev. Lett. **94**, 021601 (2005).
[59] C. Alexandrou, G. Koutsou, H. Neff, J. W. Negele, W. Schroers, and A. Tsapalis, Phys. Rev. D **77**, 085012 (2008).
[60] M. De Sanctis, M. M. Giannini, E. Santopinto, and A. Vassallo, Nucl. Phys. **A755**, 294 (2005).
[61] S. Capstick, Phys. Rev. D **46**, 1965 (1992).
[62] N. F. Sparveris *et al*. Phys. Rev. C **78**, 018201 (2008).